Biophysical *Journal*
Article

Biophysical Society

Spatially Different Tissue-Scale Diffusivity Shapes ANGUSTIFOLIA3 Gradient in Growing Leaves

Kensuke Kawade,[1,2,3,*] Hirokazu Tanimoto,[4] Gorou Horiguchi,[5,6] and Hirokazu Tsukaya[1,7]
[1]Okazaki Institute for Integrative Bioscience, [2]National Institute for Basic Biology, and [3]Department of Basic Biology, School of Life Science, Graduate University for Advanced Studies (SOKENDAI), Okazaki, Aichi, Japan; [4]Institut Jacques Monod, Paris, France; [5]Department of Life Science, College of Science and [6]Research Center for Life Science, Rikkyo University, Tokyo, Japan; and [7]Department of Biological Sciences, Graduate School of Science, University of Tokyo, Tokyo, Japan

ABSTRACT The spatial gradient of signaling molecules is pivotal for establishing developmental patterns of multicellular organisms. It has long been proposed that these gradients could arise from the pure diffusion process of signaling molecules between cells, but whether this simplest mechanism establishes the formation of the tissue-scale gradient remains unclear. Plasmodesmata are unique channel structures in plants that connect neighboring cells for molecular transport. In this study, we measured cellular- and tissue-scale kinetics of molecular transport through plasmodesmata in *Arabidopsis thaliana* developing leaf primordia by fluorescence recovery assays. These trans-scale measurements revealed biophysical properties of diffusive molecular transport through plasmodesmata and revealed that the tissue-scale diffusivity, but not the cellular-scale diffusivity, is spatially different along the leaf proximal-to-distal axis. We found that the gradient in cell size along the developmental axis underlies this spatially different tissue-scale diffusivity. We then asked how this diffusion-based framework functions in establishing a signaling gradient of endogenous molecules. ANGUSTIFOLIA3 (AN3) is a transcriptional co-activator, and as we have shown here, it forms a long-range signaling gradient along the leaf proximal-to-distal axis to determine a cell-proliferation domain. By genetically engineering AN3 mobility, we assessed each contribution of cell-to-cell movement and tissue growth to the distribution of the AN3 gradient. We constructed a diffusion-based theoretical model using these quantitative data to analyze the AN3 gradient formation and demonstrated that it could be achieved solely by the diffusive molecular transport in a growing tissue. Our results indicate that the spatially different tissue-scale diffusivity is a core mechanism for AN3 gradient formation. This provides evidence that the pure diffusion process establishes the formation of the long-range signaling gradient in leaf development.

INTRODUCTION

Many developmental patterns are critically dependent on spatial gradients of signaling molecules in multicellular organisms. A seminal work theoretically postulated that pure diffusion of signaling molecules from a restricted source is sufficient to establish such tissue-scale gradients (1). Despite the prominence of this diffusion-based framework in development (2,3), quantitative studies, mainly conducted in animal developmental systems, have not yet demonstrated this hypothetical model in multicellular tissues. This is due to complex processes involved in morphogen transport in animals, such as interactions with proteoglycans, that influence the tissue-scale mobility of signaling molecules, in addition to rapid extracellular diffusion (4–6). This complex interplay makes it difficult to link cellular-scale molecular transport with tissue-scale mobility to understand signaling-gradient formation. Given this situation, the diffusion-based model is still restricted in a *Drosophila Bicoid* (*Bcd*) gradient within a syncytium, a single multinucleated cell without growth (7–12).

In plants, some signaling molecules form such long-range gradients by intercellular mobility to determine the cell-proliferation domain (13,14). Tissue growth is also proposed to be involved in the spread of signaling molecules through cell-lineage transport (14–19). It is thus important to quantitatively evaluate these two modes of molecular transport to address how tissue-scale signaling gradients are formed in a growing tissue. However, integrative approaches using quantitative imaging and theoretical analyses to precisely explain the mechanism of the gradient formation in plants are largely limited (14,20,21).

Submitted February 16, 2017, and accepted for publication June 29, 2017.
*Correspondence: kawa-ken@nibb.ac.jp
Kensuke Kawade and Hirokazu Tanimoto contributed equally to this work.
Editor: Anatoly Kolomeisky.
http://dx.doi.org/10.1016/j.bpj.2017.06.072

Leaves of *Arabidopsis thaliana* (*Arabidopsis*) is one model system used to experimentally and theoretically examine tissue patterning in plants (22–25). The flat leaf tissue is composed of essentially immobile cells surrounded by rigid cell walls. Quantitative imaging would be possible in this tissue because of its moderate size (~200 μm in length, corresponding to 30–50 cells). Interestingly, plasmodesmata, cellular channel structures unique to plants, directly connect neighboring cells to facilitate non-selective molecular trafficking (26–28). The aperture size of plasmodesmata and molecular size are well established as critical elements to determine molecular mobility through plasmodesmata (26–28). This simple mode of molecular transport suggests that developing leaf tissue could be a potential morphogenetic field, in which the diffusion-based framework is working. Thus, it is of great interest to test this hypothesis by linking tissue-scale molecular mobility with its cellular-scale kinetics by quantitative imaging in leaves. This would uncover whether the general framework of the diffusion-based model is viable in developmental patterning of multicellular organisms.

Cell-proliferation activity is uniform in an entire part of the *Arabidopsis* leaf primordia at a very young stage and is then arrested from the distal part, followed by post-mitotic cell differentiation. The cell-proliferation domain is maintained at a constant distance from the junction between leaf blade and petiole during early leaf development (29–34). ANGUSTIFOLIA3 (AN3, also called GRF-INTERACTING FACTOR1) is a transcriptional co-activator that activates cell proliferation in the leaf primordia (35,36). The *an3* mutant shows defective cell proliferation, in which cell number is decreased by >70% compared with the wild-type (WT) (35). On the other hand, overexpression of *AN3* activates cell proliferation, resulting in larger leaves (35). It has been revealed that AN3 is incorporated into chromatin remodeling complexes to modulate a broad spectrum of gene expression involved in the transition from cell proliferation to cell differentiation (37,38). At the molecular level, AN3 plays a pivotal role in regulating cell-proliferation activity in leaf primordia and hence in leaf tissue patterning. However, it remains unclear how AN3 regulates the spatiotemporal dynamics of cell proliferation in leaves, because cell proliferation occurs more broadly than a tissue where the *AN3* gene is expressed (26,35).

Here, we measured tissue- and cellular-scale molecular mobilities in the leaf primordia by fluorescence recovery assays using green fluorescent protein (GFP) to characterize biophysical properties of non-selective macromolecular trafficking through plasmodesmata. Based on these quantitative data, we constructed a diffusion-based theoretical model that connects cellular-scale molecular trafficking to tissue-scale distribution. This model was then applied to the endogenous signaling molecule AN3, which was shown, in this study, to form a long-range gradient along the leaf proximal-to-distal axis to determine the cell-proliferation domain. In combination with this theoretical analysis, we experimentally evaluated each contribution of intercellular mobility and cell-lineage transport of AN3 by genetically engineering AN3 mobility. Our experimental and theoretical approaches demonstrated that pure diffusion in a growing tissue is sufficient to explain AN3 gradient formation, and they therefore suggested a core mechanism for determination of the cell-proliferation domain in growing leaf tissue.

MATERIALS AND METHODS

Plant materials and growth conditions

The *Arabidopsis* WT line used in this study was Colombia-0. The *35S::GFP* line was established using a previously reported vector (39) by the floral dip method (40). The *an3-4/pAN3::AN3-GFP* and *an3-4/pAN3::AN3-3xGFPs* lines have been described elsewhere (41). Plants were grown on rockwool at 22°C under a 16-h light (fluorescent illumination at ~50 μmol m^{-2} s^{-1})/8-h dark cycle and watered daily with 0.5 g L^{-1} Hyponex solution (Hyponex, Osaka, Japan).

Square fluorescence recovery after photobleaching assay

First, leaf primordia dissected from 6- or 10-day-old *35S::GFP* seedlings were soaked in phosphate-buffered saline (PBS) on a glass slide. Microscopic observation was performed from the adaxial side of the leaf primordia using a coverslip (24 × 36 mm, thickness no. 1, 0.12–0.17 mm; Matsunami, Osaka, Japan).

Microscopy was performed using a confocal laser-scanning microscope with an objective lens Plan-Apochromat 20×/0.75 NA and a 488-nm Argon laser on standby (LSM510 equipped with a META device; Carl Zeiss, Oberkochen, Germany). The pinhole was set to 120 μm in diameter, which yields a 10-μm optical slice in this condition. Fifteen z-stack images of size 512 × 512 pixels were acquired at 2-μm steps and 5-min intervals before and after photobleaching over a 95-min period. The laser intensities were 100% and 7% for photobleaching and time-lapse imaging, respectively. A subepidermal cell plane was selected from z-stack collections for image analysis. We confirmed that leaky fluorescence from adjacent cell layers was undetectable. A region of interest (ROI) that was 54 × 54 μm was photobleached for the square fluorescence recovery after photobleaching (FRAP) assay. A one-dimensional profile of GFP fluorescence intensity along the leaf proximal-to-distal and medial-to-lateral axes was defined as an average intensity over a width of 18.4 μm. Because this analysis region was 18 μm away from the ROI edge along the leaf proximal-to-distal axis, GFP movement perpendicular to the axis was negligible in our observation time span. The averaged intensity was normalized by GFP fluorescence intensity outside of the ROI. The boundary between the GFP-positive and GFP-negative regions was defined by a threshold fluorescence intensity of 5.0 a.u. to quantify the GFP recovery as velocity. This value corresponded to 5–10% of GFP fluorescence intensity in the non-photobleached region.

All image analyses and numerical simulations, unless otherwise described, were conducted using customized scripts written in MATLAB software, R2012b, with Statistics and Machine Learning Toolbox, Image Processing Toolbox, Optimization Toolbox, and Curve Fitting Toolbox (The MathWorks, Natick, MA).

Single-cell FRAP assay

Leaf samples were prepared and imaged as described in Square FRAP Assay. An ROI within a cell was used for photobleaching. The GFP

intensity in the photobleached cell was measured manually for each time point. Experimental data from the single-cell FRAP assay (from 0 to 45 min after photobleaching) was fitted by an exponential function as

$$I(t) = (I_0 - I_{\max})e^{(-t/\tau)} + I_{\max}, \quad (1)$$

where $I(t)$ and I_0 are GFP fluorescence intensities at time t and just after photobleaching, respectively; $I_{\max}$ is a maximal GFP fluorescence intensity, determined directly from the time-course data; and τ is a time constant of GFP diffusivity. I_0 and τ are free parameters and are determined by minimizing the residual sum of squares. We confirmed that the time constant of GFP diffusivity in the leaf lower half was not larger than that in the upper half when we analyzed the data from the single-cell FRAP assay from 0 to 95 min after photobleaching using the exponential function

$$I(t) = (I_0 - I_{\text{conv}})e^{(-t/\tau)} + I_{\text{conv}}, \quad (2)$$

where I_{conv} is a free parameter for the convergence value of GFP fluorescence recovery during observation (Fig. S2 *A*). I_{conv}, in addition to I_0 and τ, was determined by minimizing the residual sum of squares.

Given that GFP fluorescence was stably recovered in a single-exponential manner throughout observation in our single-cell FRAP assay, we judged that GFP trafficking through plasmodesmata was not perturbed by, e.g., plasmodesmata gating due to damages by tissue excision and/or photobleaching treatment. Indeed, a similar timescale of protein diffusivity through plasmodesmata was observed in other published works, in which protein diffusivities were non-invasively measured using the photoconvertible fluorescence protein Dendra2 (26 kDa) and its fusion protein (42,43).

Measurement of the projected cell area

Subepidermal palisade cells in the images of the square FRAP assay at the leaf upper and lower halves were outlined as shown (Fig. 3 *A*) to measure the projected area. Each cell position in the image was determined by a centroid, represented as pixel coordinates. This image analysis was performed using custom MATLAB script (described below). Spatial distribution of cell size along the leaf proximal-to-distal axis was estimated from these independent photographs. Cell length was measured by ImageJ software at an arbitrary part of a cell in the leaf upper and lower halves using the same image sets as for the square FRAP assay (http://imagej.nih.gov/ij/).

Quantification of AN3-GFP and AN3-3xGFPs distributions

The first leaf primordia were dissected from the 6-day-old *an3-4/pAN3::AN3-GFP* and *an3-4/pAN3::AN3-3xGFPs* lines and subjected to confocal microscopy (LSM510 equipped with a META device; Carl Zeiss). Subepidermal tissue in the adaxial side was selected for observation of AN3-GFP and AN3-3xGFPs signals. We observed three independent lines for AN3-GFP and AN3-3xGFPs distributions and obtained reproducible results.

We developed a MATLAB package that allowed us to interactively measure the GFP fluorescence intensity and cellular parameters from the confocal images. The outlines of cells or nuclei were determined manually based on the fluorescence signal. The results were displayed in another window, which enabled us to check and correct the segmentation. The fluorescence intensity, projected area, and centroid of the cells or nuclei, represented as pixel coordinates, were determined automatically. More than 1450 nuclei from 12 independent leaves were analyzed for AN3-GFP and AN3-3xGFPs intensity.

Detection of nuclei in S-phase cells by EdU absorption experiment

Six-day-old seedlings were cut at the hypocotyls, and above-ground parts were floated on 10-μM 5-ethynyl-2′-deoxyuridine (EdU) solution for 3 h under normal growth conditions. Detection of EdU was performed as described elsewhere (44). The subepidermal palisade cells were examined by confocal microscopy as described above. Since cells showed a polygonal shape in the leaf primordia, the observed fluorescence was derived just from the dividing cells, not from the endoreduplicating cells.

Mathematical models and simulations

We here summarized our mathematical models and simulation methods. More details are described in the Supporting Material.

Model setup: We considered a simplified one-dimensional geometry to simulate the tissue-scale GFP mobility (Fig. S3) and the AN3 gradient formation along the proximal-to-distal axis of a growing leaf tissue (Fig. S4). Our models consist of discrete cells in which synthesis and degradation of a signaling molecule and its diffusive transport between neighboring cells occur. We directly measured cell-size distribution based on the experimental observations (Figs. 3 *B* and S2 *D*) and incorporated it into the models to analyze the tissue-scale molecular dynamics in a realistic spatial field. All parameters for the simulations are summarized in Tables S1–S3.

Molecular synthesis and degradation: We assumed that GFP synthesis and degradation are negligible in the timescale of our model for tissue-scale GFP mobility based on the experimental observations in the square and single-cell FRAP assays (Figs. S1, *A* and *B*, and S2 *B*).

In contrast, to model the AN3 gradient formation, we considered that AN3 is produced and maintained at a constant level in time within the source cells at the proximal boundary. The number of the source cells was determined by analyzing the AN3-3xGFPs gradient (Fig. 5 *C*). We investigated the degradation process with our model using a wide range of the degradation constant and found that the AN3 gradient could not be achieved if we included active degradation (Fig. S7). This is intuitively consistent with the longer timescale of the AN3 gradient formation. Based on these data, we considered that protein degradation is negligibly small in the AN3 gradient formation.

Diffusive molecular transport: We focused on molecular movement across the cell-cell boundary through plasmodesmata, because movement in the cytoplasm was much faster, so that the intracellular molecular profile was kept uniform (Fig. 2 *A*). Molecular transport was modeled as Fick's law of diffusion, where the molecular flux across the cell-cell boundary is proportional to a difference in molecular concentration between these cells. Because the kinetic constant was experimentally measured by the single-cell FRAP assay (Fig. 2 *C*), a change in plasmodesmata pattern, if there was any, was intrinsically implemented in our simulations.

Tissue growth mediated by cell division: Although the timescale for the tissue-scale GFP mobility was ~45 (or ~90) min, that for the AN3 gradient formation was ~48 h. Because the cell cycle of leaf cells at the stage we considered is ~16 h (31,45), tissue growth mediated by cell division occurs in the AN3 gradient formation but not in the tissue-scale GFP movement.

RESULTS

Tissue-scale molecular mobility is spatially different along the leaf proximal-to-distal axis

We first characterized tissue-scale molecular mobility using *Arabidopsis* leaf primordia constitutively expressing a gene encoding a GFP (molecular mass, 27 kDa) as a model system for molecular transport through the plasmodesmata. In our square FRAP assay, GFP fluorescence was

irreversibly photobleached in a rectangular ROI corresponding to ~50 cells (Fig. 1 *A*). After photobleaching, the intensity of GFP fluorescence was scanned from the proximal to the distal parts of the observed region (Fig. 1 *A*; Movie S1). Recovery of GFP fluorescence at the center of the ROI was undetectable, at least until 45 min after photobleaching (Fig. S1, *A* and *B*), suggesting that de novo GFP synthesis and GFP influx into the ROI plane across cell layers was negligible in this timescale and that the recovery of GFP fluorescence depended on the movement of GFP between cells within the same layer. We found that recovery of GFP fluorescence around the distal

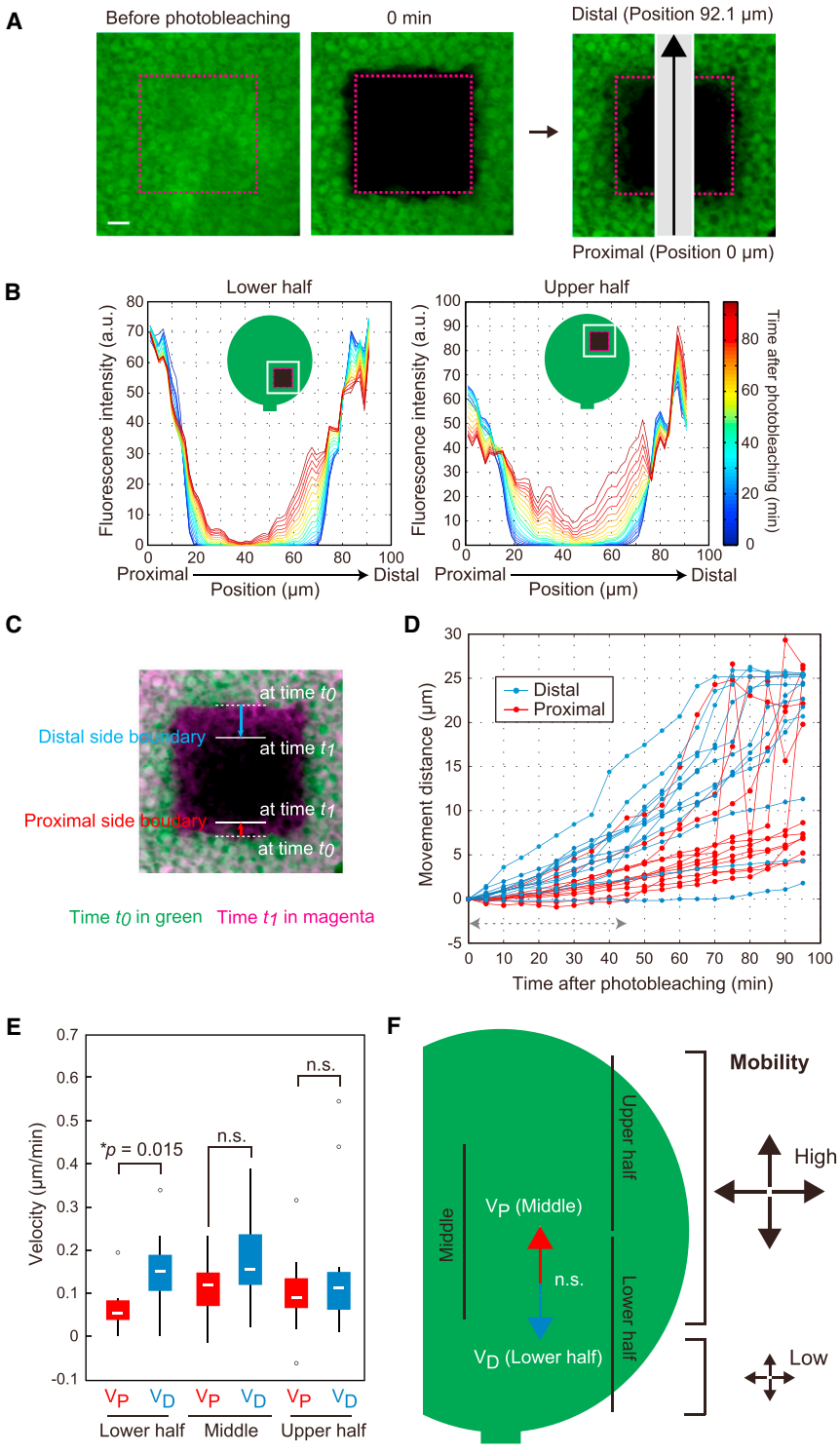

FIGURE 1 Spatial difference of tissue-scale macromolecular trafficking in leaf primordia. (*A* and *B*) Constitutively expressed GFP was photobleached in the leaf primordia (*magenta dashed box*). After photobleaching, recovery of GFP fluorescence was scanned along the leaf proximal-to-distal axis, as indicated by the gray stripe (*A*), and plotted against the position of the analysis region from the proximal to the distal end (*B*). Scale bar, 10 μm. Representative data are shown. a.u,. arbitrary unit. (*C*) Boundaries of GFP fluorescence moved inward over time (e.g., from t_0 to t_1). A representative picture at time t_0 (*green*) merged with that at time t_1 (*magenta*) is shown. Blue and red arrows indicate movement distances of the distal- and proximal-side boundaries from t_0 to t_1 as defined by threshold fluorescence intensity at 5.0 a.u. (*D*) Movement distances of the distal-side boundary (*blue*) and proximal-side boundary (*red*) in the lower half were plotted against time after photobleaching ($n = 12$). The data from 0 to 45 min after photobleaching (*dashed arrow*) were used for further analysis to avoid the effect of de novo GFP synthesis. See also Fig. S1, *A* and *B*. (*E*) V_D and V_P in the upper half, middle region, and lower half. Each box includes the data from 25 to 75%, with the horizontal line as the median. Outlying values >50% are indicated as circles. The *p* value was calculated according to the Mann-Whitney test ($n = 12$). n.s., non significant ($p > 0.05$). (*F*) V_D in the lower half and V_P in the middle region are shown as blue and red arrows, respectively. There were no significant differences between these velocities. In sum, GFP mobility occurred in a non-directional manner, but it was lower in the most proximal part of the leaf lower half. To see this figure in color, go online.

part of the ROI was greater than in the proximal part at the lower half of the leaf primordia (Fig. 1 *B*). This preferential recovery in a distal-to-proximal direction was less obvious at the upper half of the leaf primordia (Fig. 1 *B*). We did not detect any preferential recovery along the leaf medial-to-lateral axis in either the upper or lower half in the same samples (Fig. S1, *C* and *D*). These data showed that tissue-scale GFP mobility varied along the leaf proximal-to-distal axis.

In the square FRAP assay, a sharp boundary of GFP fluorescence between the ROI and the surrounding region became smooth and moved inward over time. We defined the distal- and proximal-side boundaries by threshold fluorescence intensity at 5.0 a.u. and quantified their velocities (V_D and V_P, respectively) (Fig. 1, *C* and *D*). The V_D was significantly three times greater than the V_P at the lower half (Fig. 1 *E*). There were no significant differences between V_D and V_P in the middle region or the upper half (Fig. 1 *E*). To know whether this spatial difference of tissue-scale GFP mobility is induced by preferential protein flow in the distal-to-proximal direction, we measured V_D in the lower half and V_P in the middle region within an overlapping part and found no significant differences (Fig. 1, *E* and *F*). This indicated that there was no convection dynamics of GFP mobility, nor was there preferential flow mediated by polar distribution of plasmodesmata in the distal-to-proximal direction. The GFP fluorescence recovered in a non-preferential manner at the lower half when we examined older leaf primordia in which cell proliferation was entirely arrested (Fig. S1, *E* and *F*). We thus concluded that tissue-scale GFP mobility in the most proximal part of the leaf primordia was significantly slower than that in the other parts (Fig. 1 *F*).

A gradient in cell size induces the spatial difference of tissue-scale diffusivity

We next examined kinetics of GFP mobility between neighboring cells using a single-cell FRAP assay, in which GFP fluorescence in a single targeted cell was irreversibly photobleached and then monitored over time (Fig. 2 *A*). Because recovery of GFP fluorescence within the targeted cell occurred uniformly (Fig. 2 *A*), intracellular movement of GFP was considered to be much more rapid than intercellular movement through the plasmodesmata. These data indicated that the kinetics of GFP fluorescence recovery was largely determined by GFP mobility through plasmodesmata. Recovery of GFP fluorescence reached the level present before photobleaching, and the kinetics were well fitted with a single exponential function (Figs. 2 *B* and S2 *A*). GFP fluorescence intensity in cells adjacent to the targeted cell was constant during the observation period (Fig. S2 *B*). These results strongly suggest that GFP mobility through plasmodesmata is a pure diffusion process. We obtained the characteristic time (τ) of the exponential GFP recovery from the fitting curves ($\tau = 22 \pm 3$ and 28 ± 6 min in the lower and upper halves, respectively) (Figs. 2 *C* and S2 *C*). Although a longer characteristic time indicates lower diffusivity, the time in the lower half was largely similar to (or was not larger than) that in the upper half (Figs. 2 *C* and S2 *C*). This result indicates that the spatial difference of tissue-scale mobility could not be explained by a difference in the cellular-scale diffusivity along the leaf proximal-to-distal axis. These data thus suggested that an additional element contributes to tissue-scale GFP mobility in leaf primordia.

Cell-proliferation activity is higher at the leaf proximal part and decreases toward the leaf distal part (30–34). This causes cell-size gradient along the leaf proximal-to-distal axis (38 ± 5 and 66 ± 10 μm^2 at the lower and upper halves, respectively) (Figs. 3, *A* and *B*, and S2 *D*). We hypothesized that tissue-scale GFP mobility is slowed down in the leaf proximal part because the cells are smaller, as GFP must pass through more plasmodesmata to travel a given distance. In other words, because the effective diffusion coefficient (D) of tissue-scale GFP mobility is described as $D \sim$ cell size/τ (μm^2/min),

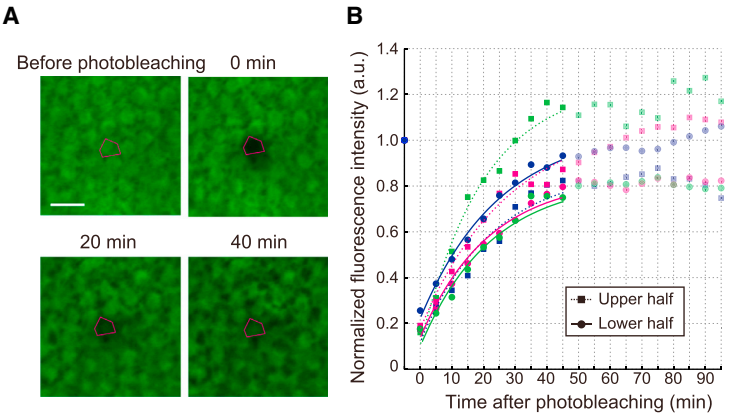

FIGURE 2 Uniform cellular-scale GFP diffusivity along the leaf proximal-to-distal axis. (*A*) Constitutively expressed GFP was photobleached in a single cell (*magenta-outlined area*). Scale bar, 10 μm. (*B*) Recovery kinetics of GFP fluorescence plotted as a function of time after photobleaching. Data for three representative leaves, with exponential fits (to the data from 0 to 45 min after photobleaching) in each leaf upper and lower half, are shown. See also Fig. S2 *A*. (*C*) Time constant of GFP diffusivity between cells in the leaf upper and lower halves. The mean ± SD are shown by the vertical lines ($n = 7$). To see this figure in color, go online.

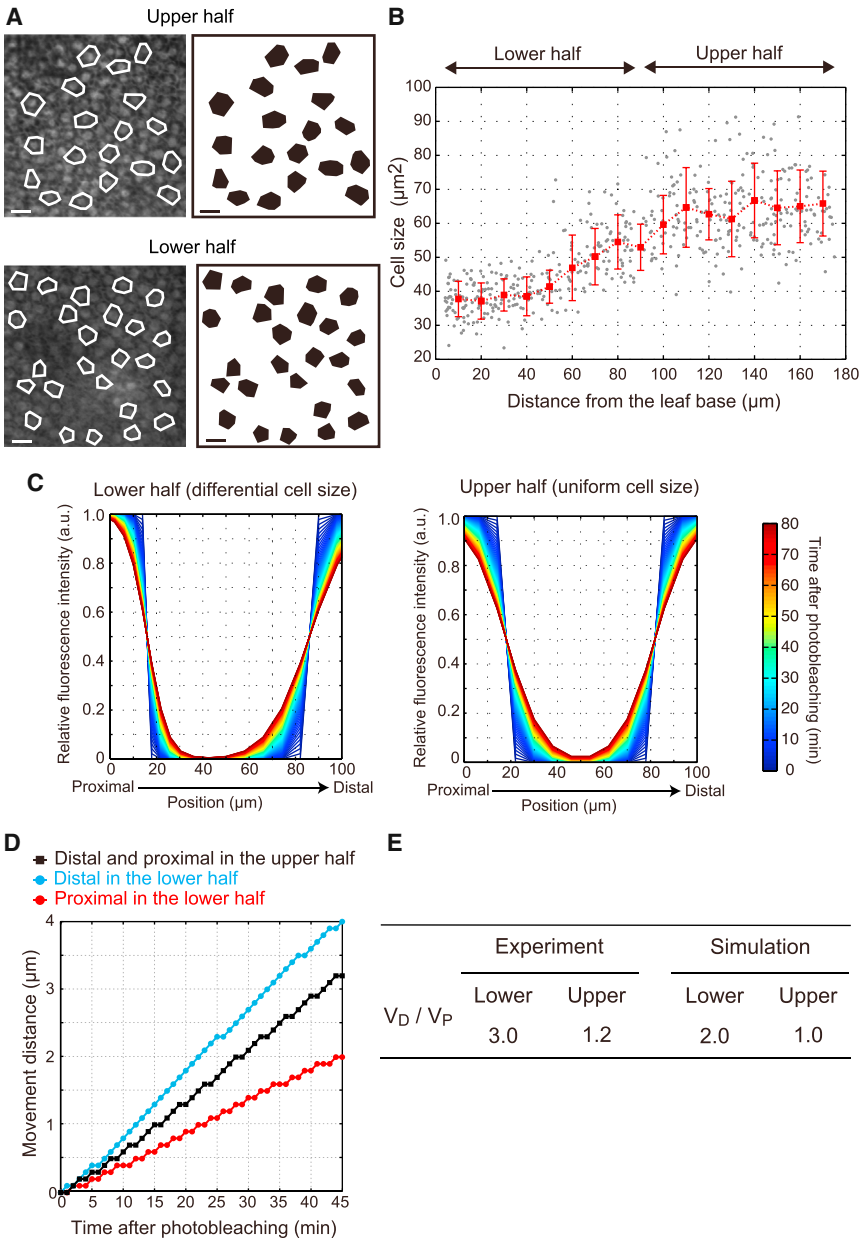

	Experiment		Simulation	
V_D / V_P	Lower	Upper	Lower	Upper
	3.0	1.2	2.0	1.0

FIGURE 3 Cell-size gradient underlies the spatially different tissue-scale GFP diffusivity. (*A*) GFP fluorescence images of subepidermal palisade cells in the leaf upper and lower halves. Representative cells are outlined in white (*left*), and their diagrams are shown (*right*). Scale bars, 10 μm. (*B*) Distribution of average cell size binned by distance at 10-μm intervals from the leaf base. The mean ± SD from more than eight independent leaf primordia (n = 16–37 cells in each position) are shown in red. Gray dots indicate each cell size. (*C*) Computed relative fluorescence intensity from our diffusion-based numerical simulation for the square FRAP assay was plotted against the relative position (see Figs. 1 *B* and S3 for summary diagrams of the simulation). a.u., arbitrary unit. (*D*) Simulated movement distance of distal- and proximal-side boundaries of the leaf upper half (*black squares*) and lower half (*blue* and *red circles*), plotted as a function of time after photobleaching. (*E*) The ratio between V_D and V_P was determined from experiment and simulation in the upper and lower halves. See also Fig. 1 *E*. All parameters used are summarized in Table S1. To see this figure in color, go online.

cell-size gradient may contribute to the spatially different tissue-scale GFP mobility. To test this hypothesis, we simulated tissue-scale GFP mobility using the measured value for GFP diffusivity between neighboring cells in uniform or differential cell-size fields along the leaf proximal-to-distal axis (see Fig. S3 for details of the simulation). We here considered simplified one-dimensional geometry, because tissue-scale GFP mobility along the leaf medial-to-lateral axis was uniform in both the upper and lower halves (Fig. S1, *C* and *D*). When we implemented the differential cell size to simulate tissue-scale GFP mobility in the lower half, V_D became two times greater than V_P, in contrast to the uniform cell-size field in the upper half (Fig. 3, *C*–*E*). This result was in good agreement with data from the square FRAP assay (Fig. 3 *E*). A difference of >2.5 in the time-constant value is required to reproduce the spatial difference of tissue-scale GFP mobility in a uniform cell-size field in the upper half (Fig. 4). Such a difference in values lies outside the 95% confidence interval of our measured data (Figs. 2 *C* and S2 *C*), further excluding the possibility that the local GFP diffusivity through plasmodesmata is modulated along the leaf proximal-to-distal axis to produce the spatial difference of tissue-scale mobility. Based on these results, we concluded that tissue-scale mobility is determined by a simple sum of diffusive transport through the plasmodesmata and that a gradient in cell size underlies the spatial difference of tissue-scale diffusivity.

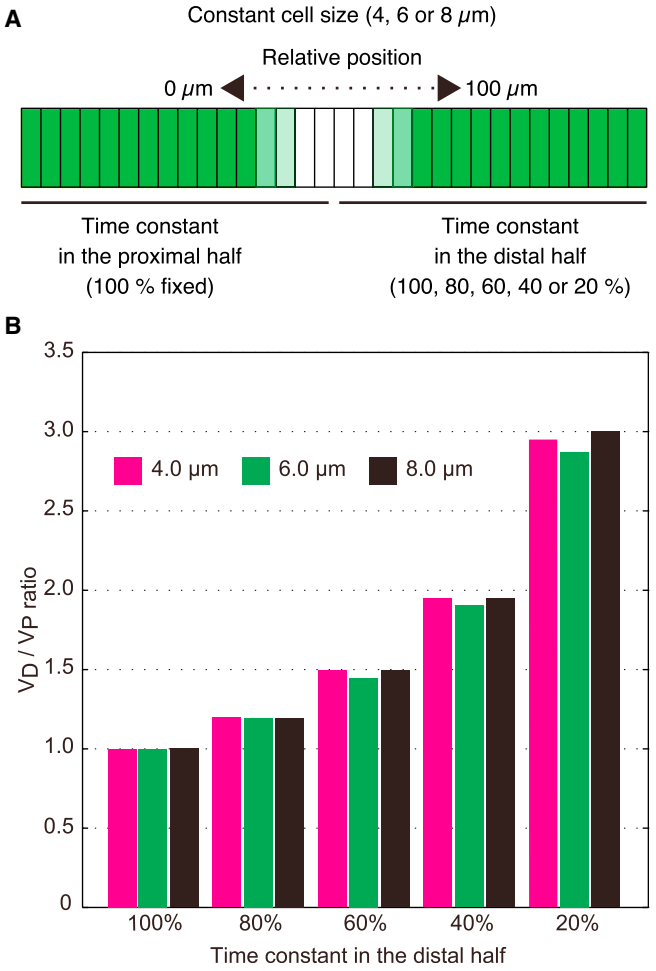

FIGURE 4 In silico perturbation experiment on local GFP diffusivity. (*A*) The time constant of GFP diffusivity in the distal half was set to 100, 80, 60, 40, or 20%, compared with that in the proximal half (100% fixed), and fluorescence recovery was computed through the constant cell-size field (4, 6, or 8 μm) over time by diffusion-based numerical simulation. See also Fig. S3. (*B*) Ratios of V_D to V_P (V_D/V_P) from the in silico experiment. Magenta, green, and black bars indicate data on 4-, 6-, and 8-μm constant-cell-size fields, respectively. The time constant in the proximal half was 2.5 times larger than that in the distal half when we used 40% as the time constant in the distal half. To see this figure in color, go online.

A pure diffusion process is a core mechanism in establishing the AN3 signaling gradient

To examine how a spatial difference of tissue-scale diffusivity works for gradient formation of endogenous signaling molecules and its developmental relevance, we examined the transcriptional co-activator AN3 (molecular mass, 22 kDa) (35–38). The *AN3* promoter is active within the most proximal part of the leaf primordia, whereas the cell-proliferation domain is formed more broadly in the distal part (26,35). One potential explanation for this spatial inconsistency is that AN3 moves along the leaf proximal-to-distal axis from the localized source, in addition to the inner-to-outer axis (41). To investigate AN3 mobility, we observed spatial distribution of AN3 in leaf primordia using *an3-4* transgenic lines expressing AN3 fused with GFP (AN3-GFP) or fused tandemly with three GFPs (AN3-3xGFPs) under the control of the functional *AN3* promoter (*an3-4/pAN3::AN3-GFP* and *an3-4/pAN3::AN3-3xGFPs*, respectively) (41). In contrast to the AN3-GFP, the AN3-3xGFPs is not capable of moving between cells due to its larger molecular size (41,46), suggesting that AN3 protein transport is mediated through plasmodesmata. The *AN3-GFP* expressed by the *AN3* promoter rescues the cell-proliferation defect in the *an3-4* genetic background, resulting in normal leaf size comparable to the WT, in the *an3-4/pAN3::AN3-GFP* (41). Although constitutively expressed *AN3-3xGFPs* by *cauliflower mosaic virus 35S* promoter also could complement the defective proliferation and smaller leaf size in the *an3-4* genetic background, the *an3-4/pAN3::AN3-3xGFPs* shows defective proliferation and smaller leaves compared to the WT (41,46). When we compared the distribution patterns of these AN3-GFP and AN3-3xGFPs, the AN3-GFP signal was broader than that of AN3-3xGFPs (Fig. 5 *A*), indicating that AN3-GFP moved between cells along the leaf proximal-to-distal axis. To investigate whether the AN3 movement contributed to establishing the cell-proliferation domain, we examined the distribution of proliferating cells in both lines. Premature arrest of cell proliferation was detected specifically in the leaf distal part of *an3-4/pAN3::AN3-3xGFPs*, when compared to *an3-4/pAN3::AN3-GFP* (Fig. 5 *B*). This result indicated that AN3 forms a graded distribution along the leaf proximal-to-distal axis through mobility to regulate the proliferation domain.

Lastly, based on the spatial difference of tissue-scale diffusivity, we quantitatively analyzed the AN3-GFP and AN3-3xGFPs distributions along the leaf proximal-to-distal axis to examine AN3 gradient formation. The AN3-3xGFPs was produced in a restricted source tissue and transported by dilution, through cell proliferation, away from the source (cell-lineage transport). In this scheme, the AN3-3xGFPs level becomes half after cell division in the target tissue, but due to subsequent cell growth, its distribution length is doubled along the developmental axis when the one-dimensional geometry is considered. An expression gradient established solely by cell-lineage transport in the targeted tissue is thus inversely proportional to the number of cells from the source tissue. This is theoretically proposed to follow a power-law form as

$$C(x) = a/x, \tag{3}$$

where a is a constant value, x is the cell number away from the leaf base, and $C(x)$ is the intensity of AN3-3xGFPs at position x (14–19,47) (see Fig. S4 A for details). To compare this theoretical prediction with the in vivo AN3-3xGFPs distribution, we quantified the expression profile of AN3-3xGFPs along the leaf proximal-to-distal axis. Fluorescence intensity was maintained at a high level from the first to fifth

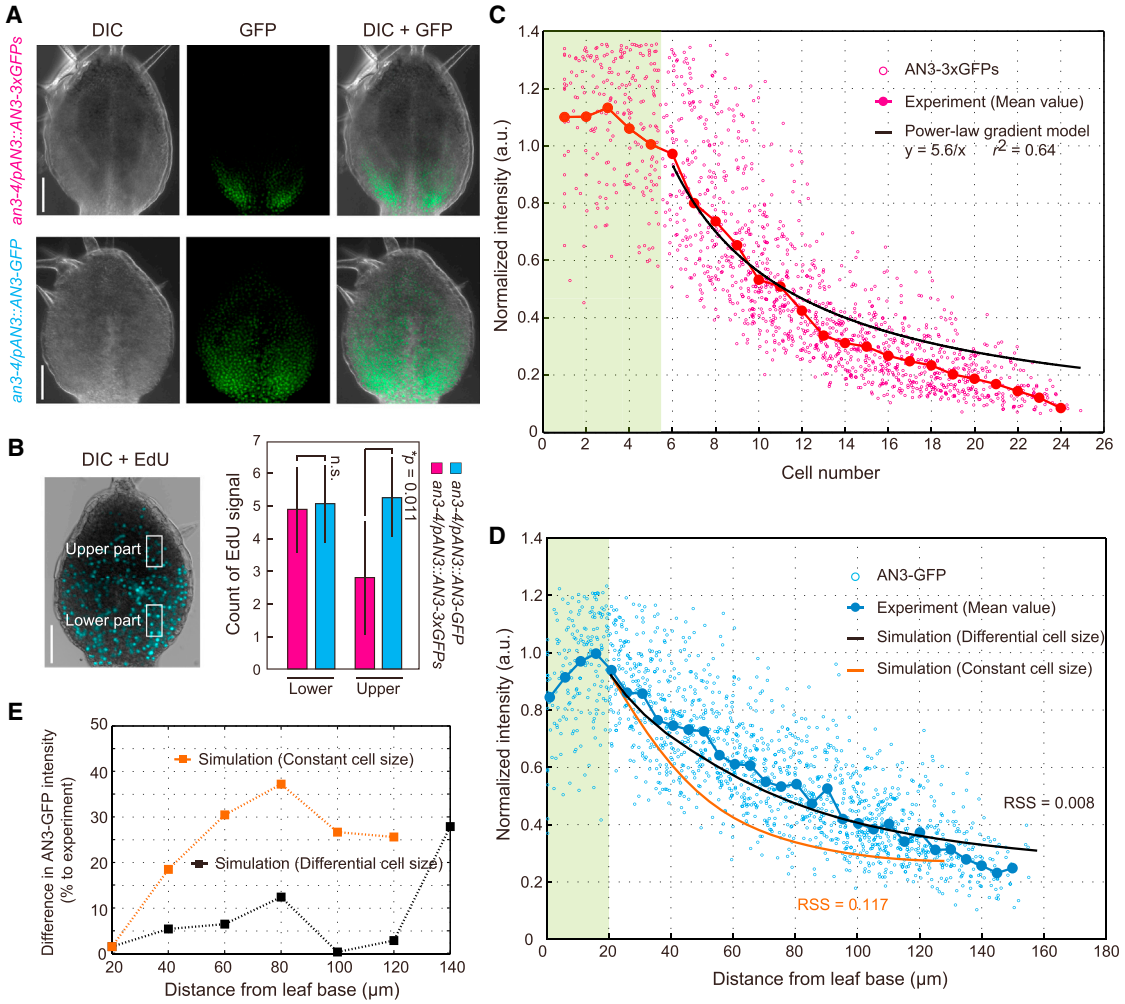

FIGURE 5 AN3 gradient formation by pure diffusion process in a growing leaf tissue. (*A*) Leaf primordia from *an3-4/pAN3::AN3-3xGFPs* (*upper*) and *an3-4/pAN3::AN3-GFP* (*lower*). DIC (*left*), GFP fluorescence (*middle*), and their merged images (*right*) are shown. Scale bars, 50 μm. (*B*) Distribution of proliferating cells in leaf primordia. A DIC image merged with EdU-positive signal (*blue*) is shown (*left*). Numbers of EdU-positive nuclei per 20 × 40 μm area (*white rectangles*) at leaf lower and upper parts were counted. The mean ± SD with the *p* value from the Student's *t*-test are shown ($n > 12$). n.s., non-significant ($p > 0.05$). Scale bars, 50 μm. (*C* and *D*) Distribution profiles for AN3-3xGFPs and AN3-GFP fluorescence intensities along the leaf proximal-to-distal axis. Normalized intensities of AN3-3xGFPs (*C*) and AN3-GFP (*D*) in nuclei are plotted as a function of cell number and distance from the leaf base, respectively. The mean of AN3-3xGFPs and AN3-GFP intensities binned by cell position (*red dots* in *C*) and distance from the leaf base at 5-μm intervals (*blue dots* in *D*) are indicated. A fitting curve with a power-law gradient to the AN3-3xGFPs profile in the targeted tissue is shown in black in (*C*). Simulated curves through the 4-μm constant-cell-size field (*orange*) and the differential (from 4 to 8 μm) cell-size field (*black*) are shown in (*D*). a.u., arbitrary unit. The green shaded area indicates the region of source tissue. RSS, residual sum of squares. (*E*) Difference in AN3-GFP intensity between simulated and experimentally determined profiles. The differences of the simulated curve with 4-μm constant cell size (*orange*) and with differential cell size (*black*) against experimentally measured values are plotted as a function of the distance from the leaf base. Mean deviations were calculated based on the data for 20–120 μm from the leaf base. All parameters used are summarized in Table S2. To see this figure in color, go online.

cells (corresponding to 0–20 μm) along the axis, and dropped steeply as the distance from the leaf base increased (Fig. 5 *C*). The AN3-3xGFPs profile more than six cells away from the leaf base was well-fitted by the power-law form ($a = 5.6$, with fitting accuracy $r^2 = 0.65$; Fig. 5 *C*). These data indicated that AN3-3xGFPs was produced in the source tissue located at the most proximal part of the leaf primordia (first to fifth cells), and spread into the targeted tissue by cell-lineage transport (away from the sixth cell).

The AN3-GFP profile showed a longer-range distribution than the AN3-3xGFPs profile in the targeted tissue (Fig. 5 *D*). We performed a one-dimensional simulation for formation of an AN3-GFP gradient, in which AN3-GFP spread from a restricted source tissue by diffusive transport through plasmodesmata in combination with cell-lineage transport (see Fig. S4 for details). Using the values determined experimentally by a single-cell FRAP assay and quantitative analysis of the AN3-3xGFPs profile, our simulation summarized the AN3-GFP gradient in the targeted tissue well

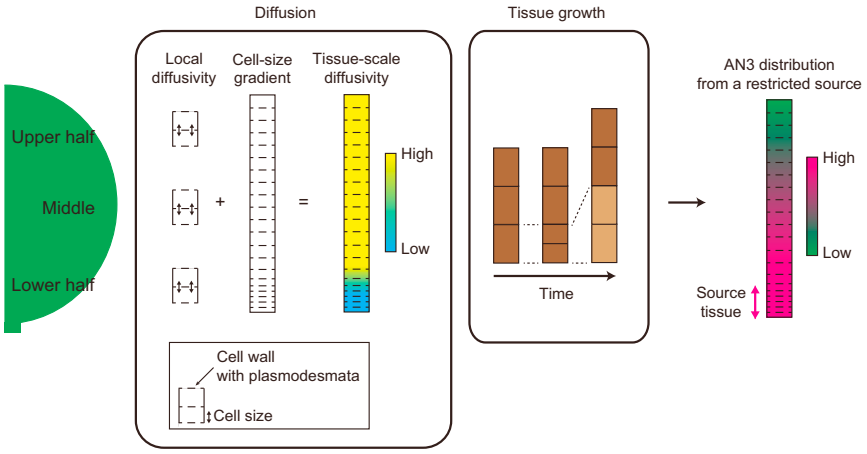

FIGURE 6 Proposed model for AN3 gradient formation. Although molecular diffusivity through plasmodesmata is uniform in the early leaf primordia, tissue-scale diffusivity is spatially varied due to smaller cell size in the most proximal part. In addition, cell-lineage molecular transport mediated by cell proliferation intrinsically occurs in a growing tissue. This spatial difference of tissue-scale diffusivity in a growing tissue is sufficient to explain how the long-range AN3 gradient from a restricted source tissue is established in leaves. To see this figure in color, go online.

(Fig. 5 *D*). Strikingly, the mean deviation between measured and simulated AN3-GFP profiles, except at the furthermost distal part, was <5% (Fig. 5 *E*). This higher reproducibility was also maintained when we used the theoretically predicted diffusivity of two tandemly fused GFPs, which is experimentally shown to be capable of moving through plasmodesmata in a non-selective fashion (28) (54 kDa, $\tau = 40$ min; mean deviation of 14%; Figs. S5 A and S6). These values were much better than those found assuming constant cell size from the leaf base (mean deviations of 23% ($\tau = 25$ min; Fig. 5, *D* and *E*) and 31% ($\tau = 40$ min; Fig. S6 A)). Therefore, we concluded that the spatial difference of tissue-scale diffusivity could be a critical mechanism for formation of the long-range AN3 gradient along the leaf proximal-to-distal axis, which further guides spatial distribution of cell-proliferation activity (Fig. 6).

DISCUSSION

We have addressed the key question of how a dynamic signaling gradient is established in a growing tissue. First, using trans-scale florescence recovery assays, we characterized the distribution of molecular diffusivity in leaf primordia and found that tissue-scale diffusivity, but not cellular-scale diffusivity, is spatially varied along the proximal-to-distal axis. Our work uncovered that the gradient in cell size underlies this phenomenon, strongly suggesting that tissue-scale molecular mobility can be described as a diffusion process if position-dependent cell size is appropriately considered. Second, by genetically engineering AN3 mobility, we quantitatively dissected the contributions of diffusive transport through the plasmodesmata and of tissue growth in establishing the AN3 gradient. Based on these data, we concluded that the simplest mechanism of diffusion could be a core determinant for the AN3 gradient formation. This is, to our knowledge, the first report linking cellular-scale diffusion to tissue-scale diffusivity, thereby showing how the long-range signaling gradient is formed along the developmental axis of compartmentalized tissue. In addition, we proposed that this signaling gradient contributes to determination of the cell-proliferation domain. We thus suggest that the diffusion equation fulfills the dynamic formation of a signaling gradient, and hence a tissue growth mechanism, as conceptualized in the seminal work of Crick (1).

Diffusion-based framework for signaling-gradient formation in a growing tissue

Most studies of signaling-gradient formation hypothesized that mobility of the signaling molecule is uniform within organ primordia. However, inhomogeneous distribution of the cell-proliferation rate occurs widely in a growing tissue in animals and plants (30,48–50). We pointed out that such a spatial difference could induce differential cell-size distribution; thereafter, it plays an important role in determination of spatially different tissue-scale diffusivity and establishment of a signaling gradient. In contrast to tissue-scale diffusivity, our data showed that cellular-scale diffusivity is uniform along the leaf proximal-to-distal axis. The characteristic time for GFP diffusivity on a cellular scale measured by the single-cell FRAP assay ($\tau = \sim$25 min) is similar to the mobility of the animal morphogen Decapentaplegic restricted by non-diffusive hindrance factors ($\tau =$ 10–30 min at the 10 μm scale), although its extracellular diffusion is much faster (τ on the order of several seconds at the 10 μm scale) (2,6). These data indicate that, in plants, diffusive molecular transport between neighboring cells through plasmodesmata is a major determinant of tissue-scale mobility, in contrast to the case for animals, in which non-diffusive processes are rate-limiting steps (2,6,51). This difference highlights that the diffusion-based framework is a critical system for signaling gradient formation in particular in plants.

Plasmodesmata shape and density might be changed depending on cellular developmental stage, as observed during the physiological transition from sink to source leaves (52,53). Plasmodesmata conductivity is also affected by

callose deposition around its neck region, which is involved in the modulation of mobility of signaling molecules (27,54,55). However, we demonstrated that local molecular transport through plasmodesmata is comparable between the upper and lower halves of leaf primordia by single-cell FRAP assay. This result indicates that changes in local molecular mobility by plasmodesmata modifications are not obvious or, if there were any, they might have canceled each other out, resulting in uniform cellular-scale diffusivity throughout the leaf primordia at this developmental stage.

Dynamics of AN3 signaling and proliferation control in leaves

Our study showed that the AN3 signaling gradient became steeper when we perturbed the AN3 mobility, resulting in premature arrest of cell proliferation in the leaf distal part. Manipulation of the *AN3* expression level by overexpression or antisense/RNA interference experiments revealed that cell-proliferation activity was well correlated with expression level in leaf primordia (35,56,57). These facts strongly suggest that the concentration gradient of AN3 plays an important role in regulating cell-proliferation dynamics along the leaf proximal-to-distal axis. We speculate that spatial difference of tissue-scale diffusivity along the leaf proximal-to-distal axis might help to maintain the higher AN3 concentration in the leaf proximal part for vigorous proliferation, and also to form long-range distribution toward the leaf distal part for lower, but detectable, proliferation activity. Despite differences in molecular components and tissue contexts, a developmental mechanism using the spatial gradient of a signaling molecule to regulate determinate tissue growth might be a preferable strategy across kingdoms.

Emerging evidence suggests that mechanical stress due to tissue growth induces feedback regulation on cell-proliferation activity in *Arabidopsis* petals and *Drosophila* wing discs (48,58,59). Given a relationship between the AN3 gradient and the proliferation activity, the shape of the AN3 gradient would be affected by mechanical feedback in response to tissue growth. Such a regulatory architecture operating in time and space has been suggested as a proprioception system for tight regulation of tissue growth (48,60–62). Our proposed framework would be a basis to consider a dynamic regulatory principle that integrates genetic and non-genetic cues for robust patterning in multicellular organisms. Because AN3 is capable of moving across cell layers (41), the inter-cell-layer mobility would affect the AN3 distribution when we consider a longer timescale. It would be interesting to test this cross talk in future work using a more complex model than our one-dimensional one that incorporates this inter-cell-layer movement and also mechanical feedback in three-dimensional geometry. Implementing the kinetics of AN3 mobility in this future model will also be helpful for further investigation of AN3 gradient formation.

SUPPORTING MATERIAL

Seven figures, three tables, and one movie are available at http://www.biophysj.org/biophysj/supplemental/S0006-3495(17)30808-1.

AUTHOR CONTRIBUTIONS

K.K. and H. Tanimoto conceived and designed the project. G.H. and H. Tsukaya helped design the project. K.K. carried out all experiments. H. Tanimoto developed the scripts for image analysis and mathematical modeling. K.K. and H. Tanimoto analyzed the data and performed the computational simulations. G.H. provided material. K.K., H. Tanimoto, G.H., and H. Tsukaya discussed the data and wrote the manuscript.

ACKNOWLEDGMENTS

We are grateful to H. Koyama and Y. Mii (National Institute for Basic Biology, Japan) for critically reading this manuscript.

This work was supported by a BIO-NEXT project from Okazaki Institute for Integrative Bioscience (to K.K. and H. Tsukaya), a grant for Basic Science Research Projects from The Sumitomo Foundation (150238) (to K.K.), Grants-in-Aid for Young Scientists (B) (15K18549) (to K.K.) and Scientific Research on Innovation Areas (25113002) (to G.H. and H. Tsukaya) from the Japan Society for the Promotion of Science.

SUPPORTING CITATIONS

References (63,64) appear in the Supporting Material.

REFERENCES

1. Crick, F. 1970. Diffusion in embryogenesis. *Nature.* 225:420–422.
2. Kicheva, A., P. Pantazis, …, M. González-Gaitán. 2007. Kinetics of morphogen gradient formation. *Science.* 315:521–525.
3. Müller, P., K. W. Rogers, …, A. F. Schier. 2012. Differential diffusivity of Nodal and Lefty underlies a reaction-diffusion patterning system. *Science.* 336:721–724.
4. Belenkaya, T. Y., C. Han, …, X. Lin. 2004. *Drosophila* Dpp morphogen movement is independent of dynamin-mediated endocytosis but regulated by the glypican members of heparan sulfate proteoglycans. *Cell.* 119:231–244.
5. Duchesne, L., V. Octeau, …, D. G. Fernig. 2012. Transport of fibroblast growth factor 2 in the pericellular matrix is controlled by the spatial distribution of its binding sites in heparan sulfate. *PLoS Biol.* 10:e1001361.
6. Zhou, S., W. C. Lo, …, A. D. Lander. 2012. Free extracellular diffusion creates the Dpp morphogen gradient of the *Drosophila* wing disc. *Curr. Biol.* 22:668–675.
7. Abu-Arish, A., A. Porcher, …, C. Fradin. 2010. High mobility of bicoid captured by fluorescence correlation spectroscopy: implication for the rapid establishment of its gradient. *Biophys. J.* 99:L33–L35.
8. Berezhkovskii, A. M., C. Sample, and S. Y. Shvartsman. 2010. How long does it take to establish a morphogen gradient? *Biophys. J.* 99:L59–L61.
9. Drocco, J. A., O. Grimm, …, E. Wieschaus. 2011. Measurement and perturbation of morphogen lifetime: effects on gradient shape. *Biophys. J.* 101:1807–1815.

10. Gregor, T., W. Bialek, …, E. F. Wieschaus. 2005. Diffusion and scaling during early embryonic pattern formation. *Proc. Natl. Acad. Sci. USA.* 102:18403–18407.
11. Gregor, T., E. F. Wieschaus, …, D. W. Tank. 2007. Stability and nuclear dynamics of the bicoid morphogen gradient. *Cell.* 130:141–152.
12. He, F., T. E. Saunders, …, J. Ma. 2010. Shaping a morphogen gradient for positional precision. *Biophys. J.* 99:697–707.
13. Matsuzaki, Y., M. Ogawa-Ohnishi, …, Y. Matsubayashi. 2010. Secreted peptide signals required for maintenance of root stem cell niche in *Arabidopsis*. *Science.* 329:1065–1067.
14. Mähönen, A. P., K. Ten Tusscher, …, B. Scheres. 2014. PLETHORA gradient formation mechanism separates auxin responses. *Nature.* 515:125–129.
15. Averbukh, I., D. Ben-Zvi, …, N. Barkai. 2014. Scaling morphogen gradients during tissue growth by a cell division rule. *Development.* 141:2150–2156.
16. Chisholm, R. H., B. D. Hughes, and K. A. Landman. 2010. Building a morphogen gradient without diffusion in a growing tissue. *PLoS One.* 5:e12857.
17. Wartlick, O., F. Jülicher, and M. Gonzalez-Gaitan. 2014. Growth control by a moving morphogen gradient during *Drosophila* eye development. *Development.* 141:1884–1893.
18. Ibañes, M., Y. Kawakami, …, J. C. Izpisúa Belmonte. 2006. Cell lineage transport: a mechanism for molecular gradient formation. *Mol. Syst. Biol.* 2:57.
19. Dubrulle, J., and O. Pourquié. 2004. fgf8 mRNA decay establishes a gradient that couples axial elongation to patterning in the vertebrate embryo. *Nature.* 427:419–422.
20. Clark, N. M., E. Hinde, …, R. Sozzani. 2016. Tracking transcription factor mobility and interaction in *Arabidopsis* roots with fluorescence correlation spectroscopy. *eLife.* 5:e14770.
21. Kuchen, E. E., S. Fox, …, E. Coen. 2012. Generation of leaf shape through early patterns of growth and tissue polarity. *Science.* 335:1092–1096.
22. Bilsborough, G. D., A. Runions, …, M. Tsiantis. 2011. Model for the regulation of *Arabidopsis thaliana* leaf margin development. *Proc. Natl. Acad. Sci. USA.* 108:3424–3429.
23. Nakamasu, A., H. Nakayama, …, S. Kimura. 2014. A developmental model for branching morphogenesis of lake cress compound leaf. *PLoS One.* 9:e111615.
24. Hayakawa, Y., M. Tachikawa, and A. Mochizuki. 2016. Flat leaf formation realized by cell-division control and mutual recessive gene regulation. *J. Theor. Biol.* 404:206–214.
25. Tsukaya, H. 2014. Comparative leaf development in angiosperms. *Curr. Opin. Plant Biol.* 17:103–109.
26. Kawade, K., and H. Tanimoto. 2015. Mobility of signaling molecules: the key to deciphering plant organogenesis. *J. Plant Res.* 128:17–25.
27. Otero, S., Y. Helariutta, and Y. Benitez-Alfonso. 2016. Symplastic communication in organ formation and tissue patterning. *Curr. Opin. Plant Biol.* 29:21–28.
28. Crawford, K. M., and P. C. Zambryski. 2001. Non-targeted and targeted protein movement through plasmodesmata in leaves in different developmental and physiological states. *Plant Physiol.* 125:1802–1812.
29. Andriankaja, M., S. Dhondt, …, D. Inzé. 2012. Exit from proliferation during leaf development in *Arabidopsis thaliana*: a not-so-gradual process. *Dev. Cell.* 22:64–78.
30. Donnelly, P. M., D. Bonetta, …, N. G. Dengler. 1999. Cell cycling and cell enlargement in developing leaves of *Arabidopsis*. *Dev. Biol.* 215:407–419.
31. Ichihashi, Y., K. Kawade, …, H. Tsukaya. 2011. Key proliferative activity in the junction between the leaf blade and leaf petiole of *Arabidopsis*. *Plant Physiol.* 157:1151–1162.
32. Kazama, T., Y. Ichihashi, …, H. Tsukaya. 2010. The mechanism of cell cycle arrest front progression explained by a *KLUH/CYP78A5*-dependent mobile growth factor in developing leaves of *Arabidopsis thaliana*. *Plant Cell Physiol.* 51:1046–1054.
33. Nath, U., B. C. W. Crawford, …, E. Coen. 2003. Genetic control of surface curvature. *Science.* 299:1404–1407.
34. White, D. W. 2006. *PEAPOD* regulates lamina size and curvature in *Arabidopsis*. *Proc. Natl. Acad. Sci. USA.* 103:13238–13243.
35. Horiguchi, G., G. T. Kim, and H. Tsukaya. 2005. The transcription factor AtGRF5 and the transcription coactivator AN3 regulate cell proliferation in leaf primordia of *Arabidopsis thaliana*. *Plant J.* 43:68–78.
36. Kim, J. H., and H. Kende. 2004. A transcriptional coactivator, AtGIF1, is involved in regulating leaf growth and morphology in *Arabidopsis*. *Proc. Natl. Acad. Sci. USA.* 101:13374–13379.
37. Vercruyssen, L., A. Verkest, …, D. Inzé. 2014. ANGUSTIFOLIA3 binds to SWI/SNF chromatin remodeling complexes to regulate transcription during *Arabidopsis* leaf development. *Plant Cell.* 26:210–229.
38. Nelissen, H., D. Eeckhout, …, G. De Jaeger. 2015. Dynamic changes in ANGUSTIFOLIA3 complex composition reveal a growth regulatory mechanism in the maize leaf. *Plant Cell.* 27:1605–1619.
39. Narita, N. N., S. Moore, …, H. Tsukaya. 2004. Overexpression of a novel small peptide ROTUNDIFOLIA4 decreases cell proliferation and alters leaf shape in *Arabidopsis thaliana*. *Plant J.* 38:699–713.
40. Clough, S. J., and A. F. Bent. 1998. Floral dip: a simplified method for Agrobacterium-mediated transformation of *Arabidopsis thaliana*. *Plant J.* 16:735–743.
41. Kawade, K., G. Horiguchi, …, H. Tsukaya. 2013. ANGUSTIFOLIA3 signaling coordinates proliferation between clonally distinct cells in leaves. *Curr. Biol.* 23:788–792.
42. Kitagawa, M., and T. Fujita. 2013. Quantitative imaging of directional transport through plasmodesmata in moss protonemata via single-cell photoconversion of Dendra2. *J. Plant Res.* 126:577–585.
43. Wu, S., K. Koizumi, …, K. L. Gallagher. 2011. Assessing the utility of photoswitchable fluorescent proteins for tracking intercellular protein movement in the *Arabidopsis* root. *PLoS One.* 6:e27536.
44. Nakayama, H., K. Kawade, …, S. Kimura. 2015. Detection of the cell proliferation zone in leaves by using EdU. *Bio Protoc.* 5:18.
45. Yin, K., M. Ueda, …, M. Umeda. 2014. A dual-color marker system for in vivo visualization of cell cycle progression in *Arabidopsis*. *Plant J.* 80:541–552.
46. Kawade, K., G. Horiguchi, and H. Tsukaya. 2010. Non-cell-autonomously coordinated organ size regulation in leaf development. *Development.* 137:4221–4227.
47. Wartlick, O., A. Kicheva, and M. González-Gaitán. 2009. Morphogen gradient formation. *Cold Spring Harb. Perspect. Biol.* 1:a001255.
48. Hervieux, N., M. Dumond, …, O. Hamant. 2016. A mechanical feedback restricts sepal growth and shape in *Arabidopsis*. *Curr. Biol.* 26:1019–1028.
49. Mao, Y., A. L. Tournier, …, N. Tapon. 2013. Differential proliferation rates generate patterns of mechanical tension that orient tissue growth. *EMBO J.* 32:2790–2803.
50. Wartlick, O., P. Mumcu, …, M. González-Gaitán. 2011. Dynamics of Dpp signaling and proliferation control. *Science.* 331:1154–1159.
51. Yu, S. R., M. Burkhardt, …, M. Brand. 2009. Fgf8 morphogen gradient forms by a source-sink mechanism with freely diffusing molecules. *Nature.* 461:533–536.
52. Oparka, K. J., A. G. Roberts, …, B. Epel. 1999. Simple, but not branched, plasmodesmata allow the nonspecific trafficking of proteins in developing tobacco leaves. *Cell.* 97:743–754.
53. Roberts, I. M., P. Boevink, …, K. J. Oparka. 2001. Dynamic changes in the frequency and architecture of plasmodesmata during the sink-source transition in tobacco leaves. *Protoplasma.* 218:31–44.
54. Han, X., T. K. Hyun, …, J. Y. Kim. 2014. Auxin-callose-mediated plasmodesmal gating is essential for tropic auxin gradient formation and signaling. *Dev. Cell.* 28:132–146.

55. Vatén, A., J. Dettmer, …, Y. Helariutta. 2011. Callose biosynthesis regulates symplastic trafficking during root development. *Dev. Cell.* 21:1144–1155.

56. Fujikura, U., G. Horiguchi, …, H. Tsukaya. 2009. Coordination of cell proliferation and cell expansion mediated by ribosome-related processes in the leaves of *Arabidopsis thaliana*. *Plant J.* 59:499–508.

57. Debernardi, J. M., M. A. Mecchia, …, J. F. Palatnik. 2014. Post-transcriptional control of *GRF* transcription factors by microRNA miR396 and GIF co-activator affects leaf size and longevity. *Plant J.* 79:413–426.

58. Hufnagel, L., A. A. Teleman, …, B. I. Shraiman. 2007. On the mechanism of wing size determination in fly development. *Proc. Natl. Acad. Sci. USA.* 104:3835–3840.

59. Schluck, T., U. Nienhaus, …, C. M. Aegerter. 2013. Mechanical control of organ size in the development of the *Drosophila* wing disc. *PLoS One.* 8:e76171.

60. Hamant, O., and B. Moulia. 2016. How do plants read their own shapes? *New Phytol.* 212:333–337.

61. Jaeger, J., D. Irons, and N. Monk. 2008. Regulative feedback in pattern formation: towards a general relativistic theory of positional information. *Development.* 135:3175–3183.

62. Shraiman, B. I. 2005. Mechanical feedback as a possible regulator of tissue growth. *Proc. Natl. Acad. Sci. USA.* 102:3318–3323.

63. Ferjani, A., G. Horiguchi, …, H. Tsukaya. 2007. Analysis of leaf development in fugu mutants of *Arabidopsis* reveals three compensation modes that modulate cell expansion in determinate organs. *Plant Physiol.* 144:988–999.

64. Haberman, W.L., and R.M. Sayre. 1958. Motion of Rigid and Fluid Spheres in Stationary and Moving Liquids inside Cylindrical Tubes. Report 1143, Department of the Navy, David Taylor Model Basin, USA.

Biophysical Journal, Volume *113*

Supplemental Information

Spatially Different Tissue-Scale Diffusivity Shapes ANGUSTIFOLIA3 Gradient in Growing Leaves

Kensuke Kawade, Hirokazu Tanimoto, Gorou Horiguchi, and Hirokazu Tsukaya

Supplemental Information

Spatially different tissue-scale diffusivity shapes ANGUSTIFOLIA3 gradient in growing leaves

Kensuke Kawade, Hirokazu Tanimoto, Gorou Horiguchi, Hirokazu Tsukaya

Contents

1. Supporting Materials and Methods

Mathematical models and simulations

(1) Tissue geometry and growth

We adopted a one-dimensional model to simulate the tissue-scale mobility of GFP in the square FRAP assay (Fig. S3) and AN3 gradient formation (Fig. S4) as differences in GFP mobility along the leaf medial-to-lateral axis were not significant (Figs. S1*C* and S1*D*). Cells were indexed from the leaf proximal part as 1, 2, …, i. We introduced parameter j to distinguish the number of cell divisions as 1, 2, …, j. Each cell had a length $L_{i;j,}$ and fluorescence intensity $F_{i;j}$, where i and j denoted the cell index and the number of cell divisions, respectively (Figs. S3 and S4).

The time span of GFP fluorescence recovery was from 0 to 45 min, so cell division would be negligible for simulation of tissue-scale GFP mobility in the square FRAP assay. In contrast, we implemented cell division for long-term simulation of the AN3 gradient formation (Fig. S4). Cells divide after each cell cycle, but kept their initial size by cell elongation, which promotes tissue growth. Protein concentration was distributed equally into the two daughter cells after cell division as;

$$F_{2i-1;j+1} = F_{2i;j+1} = F_{i;j}/2. \tag{S1}$$

(2) Protein diffusivity and degradation

Because the single-cell FRAP assay showed that intracellular movement of GFP was much more rapid than our observed timescale, we considered the GFP fluorescence intensity in a cell as a discrete and uniform single unit. Our single-cell FRAP assay revealed that protein movement through the plasmodesmata could be approximated as a pure diffusion process. The GFP influx into cell i in a given small time Δt, is thus described as a discrete event by;

$$\Delta C_i = \left\{ D_{i,i+1}\left(F_{i+1} - F_i\right) - D_{i-1,i}\left(F_i - F_{i-1}\right) \right\} \cdot \Delta t, \tag{S2}$$

where $D_{i\text{-}1,i}$ is a characteristic kinetic parameter of GFP diffusivity between cell *i-1* and *i*, which was determined by the single-cell FRAP assay (Figs. S3 and S4). We omitted the cell cycle index j to simplify the notation. With a position-independent kinetic rate of linear protein degradation k_{deg}, time-evolution of the protein concentration in the cell i is expressed as;

$$\Delta C_i = \left\{ D_{i,i+1}\left(F_{i+1} - F_i\right) - D_{i-1,i}\left(F_i - F_{i-1}\right) - k_{\deg} \cdot F_i \right\} \cdot \Delta t, \tag{S3}$$

which was solved with $\Delta t = 0.1$ sec for a total of 2^{16} steps (= 6553.6 sec) (Fig. S3).

(3) Parameters

Our simulation included the three parameters; cell length, and GFP diffusivity and degradation (Figs. S3 and S4). Cell length was estimated from the pictures used for the square FRAP assay (Fig. 3B; Fig. S2*D*). The kinetic parameter for GFP diffusivity ($D_{i\text{-}1,i}$) was determined by the single-cell FRAP assay. Because GFP fluorescence intensity in non-photobleached cells was almost constant in time in the single-cell FRAP assay (Fig. S2*B*), the characteristic time constant of the exponential recovery of GFP in a cell i (τ) and kinetic parameters $D_{i\text{-}1,i}$ and $D_{i,i+1}$ were related as;

$$D_{i-1,i} + D_{i,i+1} = 1/\tau. \tag{S4}$$

Given that the recovery kinetics of the single-cell FRAP assay exhibited weak position

dependency in the leaf primordia, there was little difference in the diffusion parameters between neighboring cells ($D_{i-1,i}$ and $D_{i,i+1}$). Thus, we determined the kinetic parameters in our simplified one-dimensional model as;

$$D_{i-1,i} = D_{i,i+1} = 1/2\tau. \quad \text{(S5)}$$

Long-term simulation of the AN3 gradient formation in growing tissue requires four additional parameters: initial setting of cell number, number of source cells that produce the AN3 protein, number of cell divisions and duration of the cell cycle (Fig. S4). We assumed that the duration of the cell cycle was 16 h, based on previous observations (1,2). The other three parameters were determined by analyzing the AN3-3xGFPs distribution (described below).

(4) Numerical simulation for the square FRAP assay

To simulate the square FRAP assay in the leaf upper and lower halves, we determined that 32 and 37 cells, respectively, have uniform relative fluorescence intensity (= 1.0) at an initial state (Fig. S3). We reproduced photobleaching in the square FRAP assay by decreasing the intensity to 0 at t = 0 in the 8 and 13 cells located at the centers of the leaf upper and lower halves, respectively. Re-distribution of GFP was investigated by numerical simulation using the experimentally determined kinetic parameter of GFP diffusivity (Fig. 2*C*). We considered that the fluorescence intensity in the cells at tissue boundaries remained constant because of the observation that photobleaching had little effect on the protein concentration in cells located far from the bleached region. We determined that k_{deg} was negligibly small (10^{-10}), as the GFP fluorescence is kept constant without *de novo* production (Fig. S1*A* and S1*B*; Fig. S2*B*). This simulation uniquely determines the value of GFP fluorescence in each cell after calculation.

(5) Numerical simulation for tissue-scale AN3-GFP and AN3-3xGFPs distributions

AN3-3xGFPs is transported solely by dilution through cell proliferation because AN3-3xGFPs is not capable of moving between cells (3,4). Thus, the distribution of AN3-3xGFPs could be approximated by the power-law form;

$$C(x) = F_0 \quad (0 \le x \le x_0), \quad \text{(S6)}$$

$$C(x) = F_0 \cdot x_1/(x - x_0) \quad (x_0 < x). \quad \text{(S7)}$$

A region where cells produce the AN3-3xGFPs but do not proliferate is indicated by x_0. To the best of our knowledge, this x_0 region has not been recognized in the leaf primordia. In addition, the power-law gradient could explain the distribution of AN3-3xGFPs when x_0 is assumed to be zero. F_0 and x_1 denoted the fluorescence intensity and size of source tissue in which cells divide and produce AN3-3xGFPs, respectively. We checked that the time span of *de novo* AN3-GFP production is negligible until 45 min after photobleaching similar to the GFP (Fig. S5*B*). In this model, the AN3-3xGFPs intensity must be related to uniformly spaced values such as cell number from the leaf base (or distance from the leaf base in constant cell-size field) since the AN3-3xGFPs could spread only by growth dilution through cell proliferation as represented by power-law form $C(x)$, which is inversely proportional to the position x. The normalized intensities of AN3-3xGFPs at the fifth and 23rd cells were 1.01 and 0.12, respectively. The ratio of these values was 0.12/1.01, which is ~ $(1/2)^3$, indicating that the concentration of AN3-3xGFPs in the source cell was diluted to $(1/2)^3$ by cell division during the gradient formation. Because there is no report of active proteolysis

of AN3-GFP and AN3-3xGFPs, the ratio indicates that cell division occurs three times during the formation of the AN3-3xGFPs gradient. We determined that the number of source cell $x_1 = 5$, based on the AN3-3xGFPs profile along the leaf proximal-to-distal axis (Fig. 5*C*). This was justified by fitting a curve of the power-law gradient to the experimental data on the AN3-3xGFPs distribution, giving $C(x) = 5.6/x$. Because $C(x_1)$ was ~1.01, we could approximate that x_1 was ~ 5.5. Because our simulation for the AN3-GFP gradient formation required an even number for the source cell number, we used $x_1 = 4$ for the initial condition of simulation. Realistic leaf length at this developmental stage (around 200 μm) could be achieved by this initial condition after uniform cell division at three times (230 μm). These estimations, together with parameters determined above, enabled us to test our model for the AN3-GFP gradient formation without parameter tuning. Thus, we could uniquely determine the value of AN3-GFP intensity in each cell. In contrast to the power-law AN3-3xGFPs gradient, we analyzed the AN3-GFP profile as a function of distance from the leaf base to incorporate cell-size gradient in our simulation model. To compare the experimentally measured and simulated values for the AN3-GFP gradient, cell index *i* was converted to distance from the leaf base based on given cell length. The cell-length distribution was determined essentially based on the experimental observation (Fig. 3*B* and S2*D*). Testing the sensitivity of degradation coefficient in our theoretical model supported the assumption that there is no active proteolysis of AN3-GFP and AN3-3xGFPs in the gradient formation. All parameters are summarized in Tables S1-S3 in the Supplemental Information.

2. Figures S1-S7

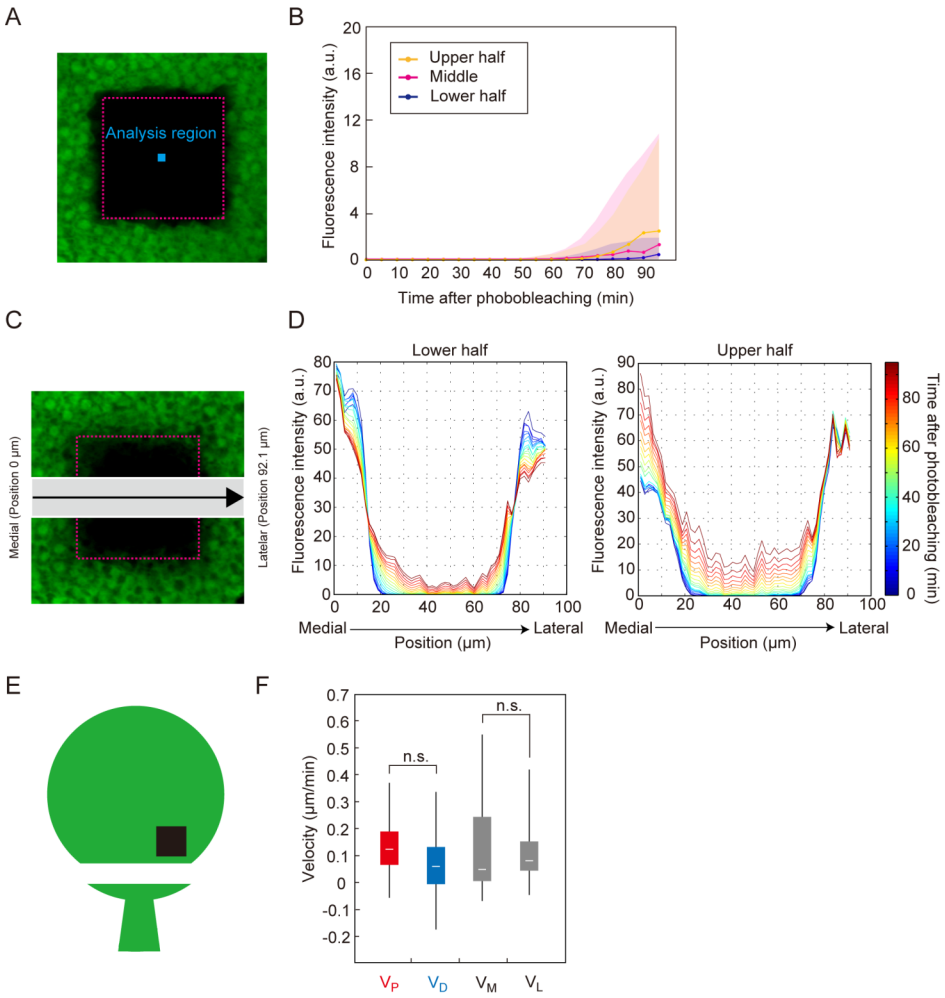

Fig. S1. Characterization of the square FRAP assay. (A and B) Fluorescence from *de novo* synthesized GFP is negligibly small. GFP fluorescence was observed in the center of the ROI [ROI, magenta dashed box; analysis region, blue (1.8 × 1.8 μm)] (A), and was plotted against time after photobleaching (B). The medians (solid line), with 25–75% values of data, are shown (B). (C and D) GFP mobility on a tissue scale is not varied along the leaf medial-to-lateral axis. Constitutively expressed GFP was photobleached (magenta dashed box) in the subepidermal palisade cells of the first leaf primordia in 6-day-old *35S::GFP* transgenic lines. Intensity of GFP fluorescence was scanned along the leaf medial-to-lateral axis [gray stripe (18.4-μm width)] over time (C), and was plotted against the position of the analysis region from medial (0 μm) to lateral (92.1 μm) (D). a.u., arbitrary unit. (E) Schematic illustration of the observed region (black square) in the square FRAP assay using older leaf primordia detached from 10-day-old *35S::GFP* lines. Cell proliferation was arrested in the entire region of the leaf primordia (5). (F) V_D and V_P, velocities of the medial side boundary (V_M) and the lateral side boundary (V_L), respectively, in the lower half of the older leaf primordia. Boxes include the data from 25 to 75% values. Horizontal line in each box shows the median value, where $n = 12$ and n.s. denotes non-significant ($p > 0.05$).

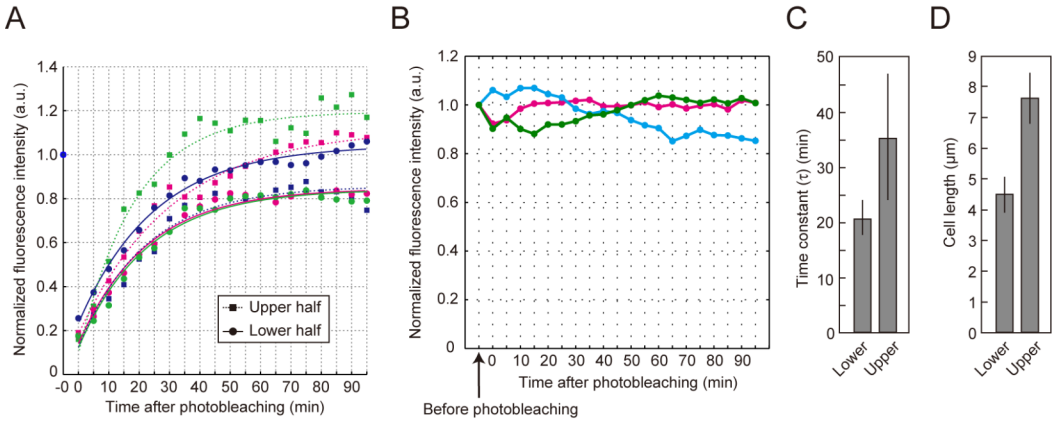

Fig. S2. Recovery kinetics of GFP fluorescence in single-cell FRAP assay from 0 to 95 min after photobleaching; and size of subepidermal cells in the leaf upper and lower halves. (A) Recovery kinetics of GFP fluorescence plotted as a function of time after photobleaching, with -0 being before photobleaching. Squares and circles show GFP fluorescence in the leaf upper and lower halves, respectively. Three representative data, with exponential fits, in each region are shown. Exponential fitting was performed using data from 0 to 95 min after photobleaching. (B) GFP fluorescence intensity in cells adjacent to the targeted cell in single-cell FRAP assay. GFP fluorescence was observed in cells adjacent to the targeted cell and plotted against time before and after photobleaching. Representative data for three independent cells are shown. (C) Time constant (τ) of GFP diffusivity between neighboring cells in the leaf upper and lower halves determined by fitting the recovery profile in (B) with a single exponential recovery. The mean ± s.d. values from seven independent experiments are shown. (D) Cell length is measured in an arbitrary portion of cells in the leaf upper and lower halves. The mean ± s.d. (n = 8–11 cells in each position) are shown.

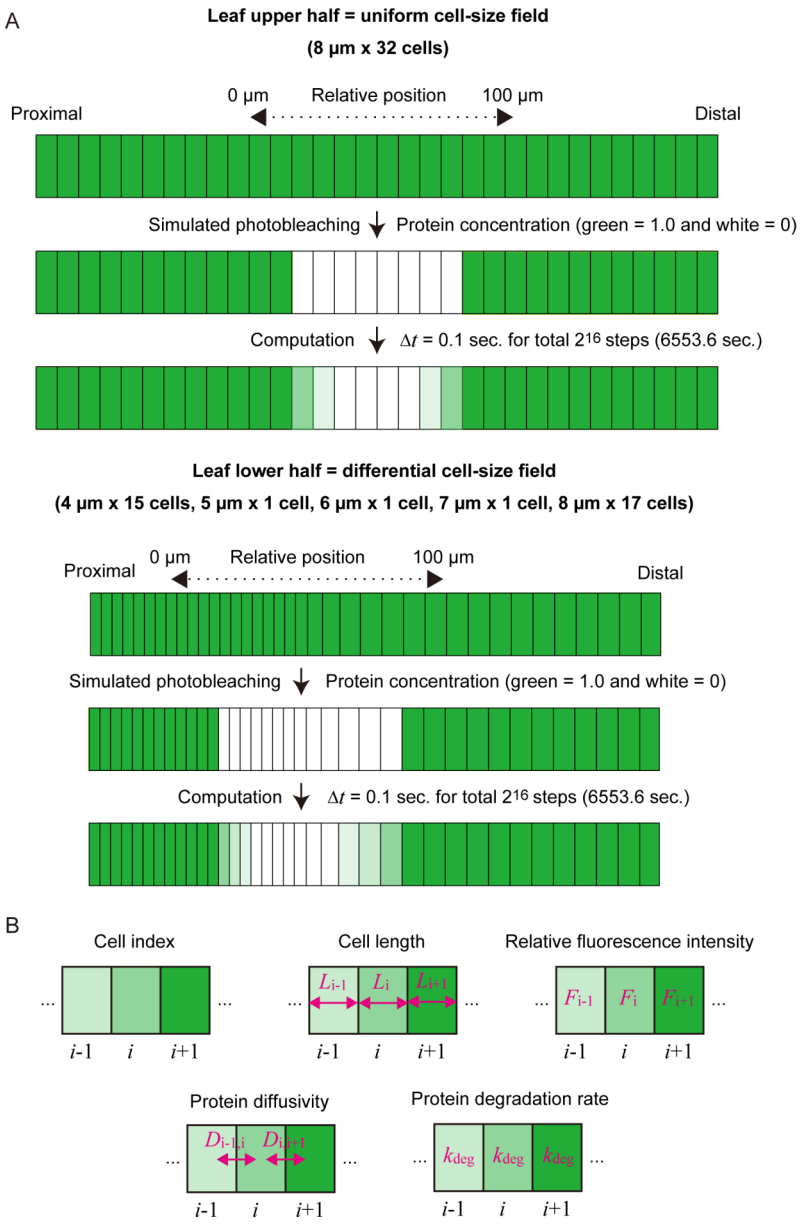

Fig. S3. Diagram of diffusion-based numerical simulation for the square FRAP assay. (A) One-dimensional geometry for simulation of tissue-scale GFP mobility in the square FRAP assay. Uniform and differential cell-size fields were prepared for the leaf upper and lower halves, respectively. Relative fluorescence intensity was then set to zero in a center of analysis area (white region) to reproduce photobleaching, followed by modeling the intensity in each cell based on protein diffusion between neighboring cells. Threshold fluorescence intensity at 0.3 a.u. was used to define the distal and proximal side boundaries. (B) Composition of the numerical simulation for the square FRAP assay. Cell index (i), cell length (L), relative fluorescence intensity (F), protein diffusivity between cells (D), and protein degradation rate (k_{deg}) are used. See *Mathematical models and simulations* section in the Supporting Materials and Methods and Table S1.

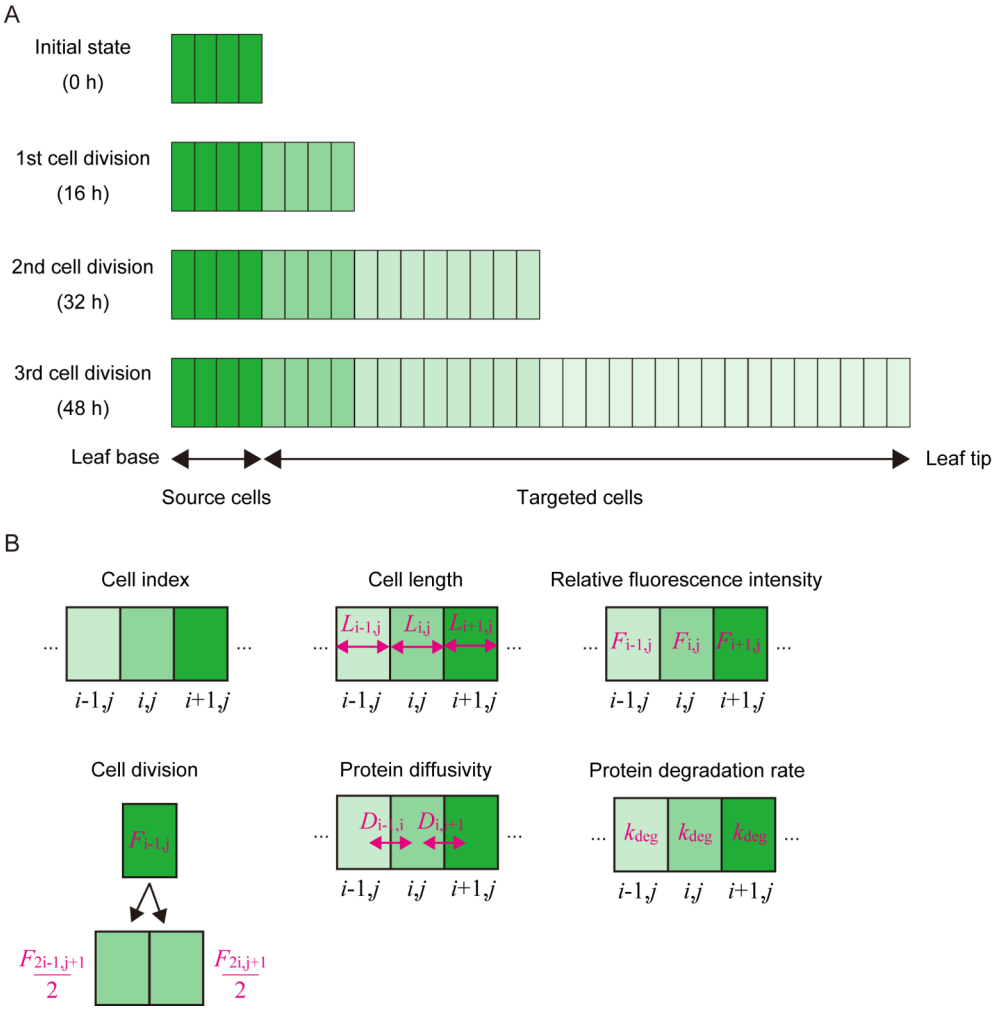

Fig. S4. Diagram of diffusion-based numerical simulation for AN3-GFP gradient formation. (A) Cell-lineage transport of AN3-GFP through targeted cells away from source cells in one-dimensional geometry. We implemented protein diffusion between neighboring cells during this cell-lineage transport for 48 h and analyzed relative fluorescence intensity along the leaf proximal-to-distal axis for simulation of AN3-GFP gradient formation. Initial state for theoretical simulations of the AN3-GFP and the AN3-3xGFPs gradients constitutes of four cells expressing AN3 at a constant level, which was determined by analyzing the AN3-3xGFPs distribution. Distance from leaf base was converted by a given cell length after the simulation to investigate an importance of differential cell-size distribution in the establishment of the AN3-GFP gradient. (B) Composition of our numerical simulation for the AN3-GFP gradient formation. Cell index (i), cell length (L), relative fluorescence intensity (F), cell division, protein diffusivity (D), and protein degradation rate (k_{deg}) were used. See *Mathematical models and simulations* section in the Supporting Materials and Methods and Table S2.

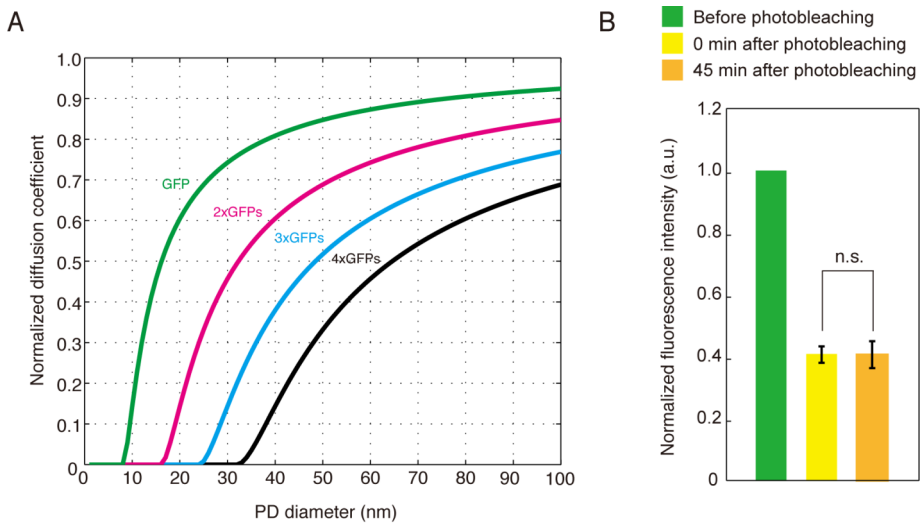

Fig. S5. Characterization of GFP diffusivity and *de novo* AN3-GFP synthesis. (A) Normalized diffusion coefficients of GFP (27 kDa), tandemly fused two GFPs (2xGFPs, 54 kDa), three GFPs (3xGFP, 81 kDa), and four GFPs (4xGFPs, 108 kDa) were estimated by a relationship between diameters of plasmodesmata (p) and spherical molecule (s), based on our previous theoretical model (6). Two parameters are involved in this model; (1) geometric effect of plasmodesmata on the permeability of the molecule (F_1),

$$F_1 = \pi(p/2 - s)^2 / \pi(p/2)^2 = (1 - 2s/p)^2, \quad \text{(S8)}$$

and (2) hydrodynamic drag force on a sphere molecule in the plasmodesmata (F_2) (7). After calculation, the normalized diffusion coefficient was plotted as a function of the plasmodesmata diameter. Because AN3-3xGFPs was not capable of moving between cells in the leaf primordia (3,4) and molecular size of 4xGFPs was close to AN3-3xGFPs (103 kDa), we presumed that the plasmodesmata diameter was less than 33 nm. Diffusivity of 2xGFPs was estimated at 62 % of the GFP diffusivity when we assumed that the plasmodesmata diameter was 30 nm. The characteristic time of 2xGFPs diffusivity between neighboring cells was 40 min under this assumption, in contrast to the GFP diffusivity, which had a characteristic time of 25 min. (B) Fluorescence from *de novo* synthesized AN3-GFP was undetectable during 45 min after photobleaching in the *an3-4/pAN3::AN3-GFP*. Square FRAP assay was performed as essentially described in Figure S1*A*. AN3-GFP fluorescence in a nucleus in a center of ROI was measured before photobleaching, just after photobleaching and 45 min after photobleaching. The mean ± s.d. values from eight independent experiments are shown. Student's *t*-test was performed (n = 8). n.s. denotes non-significant ($p > 0.05$).

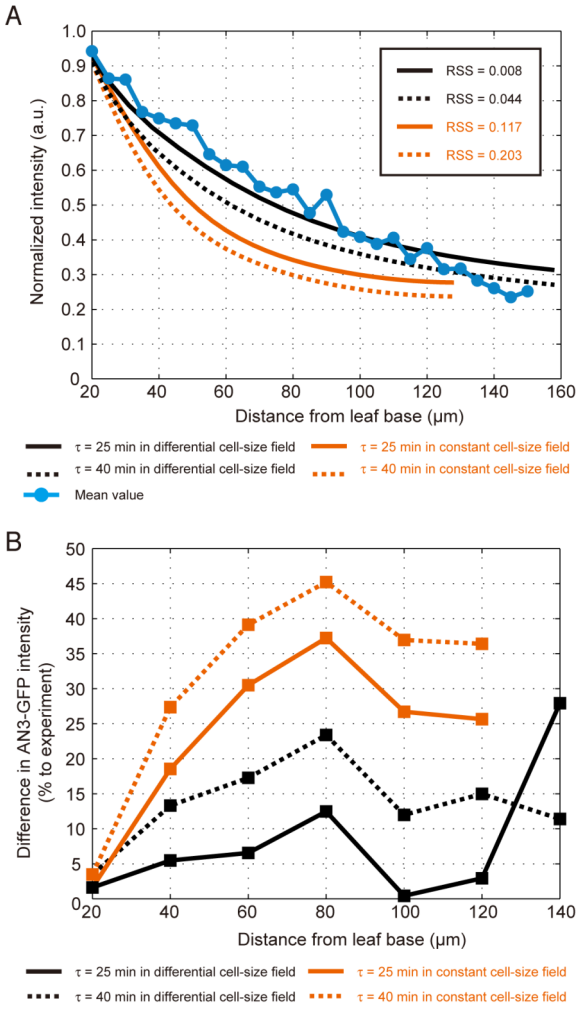

Fig. S6. Numerical simulation of AN3 gradient formation using theoretically predicted diffusivity of 2xGFPs. (A) Experimentally determined mean of AN3-GFP intensity binned by distance from the leaf base at 5-μm intervals (blue dots), simulated curves using diffusivity of GFP (characteristic time = 25 min) with 4-μm constant cell size (orange solid line), and with differential cell size from 4 to 8 μm (black solid line). In addition, we simulated the AN3-GFP gradient using diffusivity of 2xGFPs (characteristic time = 40 min), with 4-μm constant cell size (orange dashed line) and with differential cell size from 4 to 8 μm (black dashed line). (B) Difference in AN3-GFP intensity between simulated and experimentally determined profiles. The differences in simulated curves using diffusivity of GFP (characteristic time = 25 min), with 4-μm constant cell size (orange solid line) and differential cell size from 4 to 8 μm (black solid line), and using diffusivity of 2xGFPs (characteristic time = 40 min) with 4-μm constant cell size (orange dashed line) and with differential cell size from 4 to 8 μm (black dashed line) against experimentally measured values are plotted as a function of distance from the leaf base. Mean deviations were calculated based on the data from 20 to 120 μm from the leaf base. a.u., arbitrary unit. See *Mathematical models and simulations* section in the Supporting Materials and Methods. All parameters used are summarized in Table S3

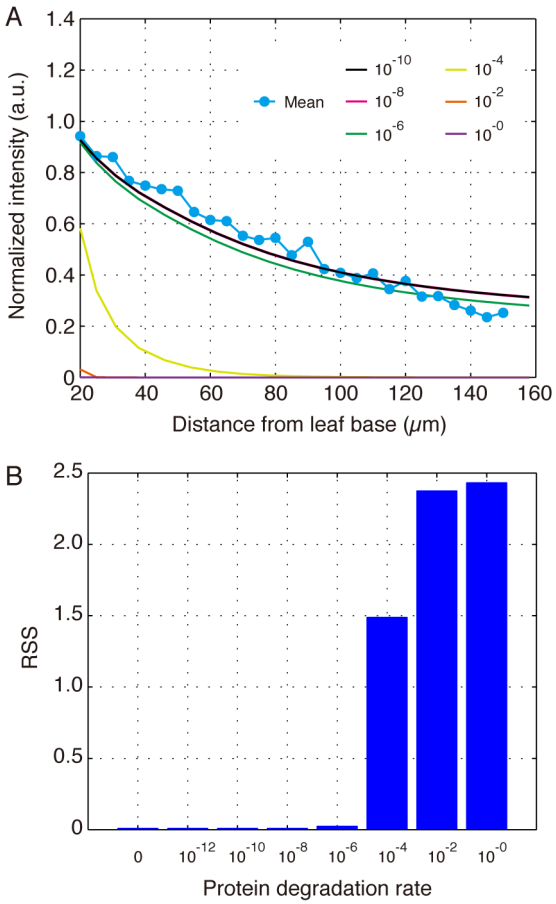

Fig. S7. Sensitivity of AN3 gradient formation to protein degradation. (A) Experimentally determined mean of AN3-GFP intensity binned by distance from the leaf base at 5-μm intervals (blue dots) and simulated curves using various protein degradation coefficients from 10^{-0} to 10^{-10}. Numerical simulation was performed with characteristic time = 25 min and differential cell size from 4 to 8 μm. (B) Difference in AN3-GFP distribution between simulated and experimentally determined profiles represented as residual sum of square.

3. Tables S1-S3

Table S1. Parameters used for the simulation of the square FRAP assay.

Time constant in the leaf upper half	28 min
Time constant in the leaf lower half	22 min
Degradation coefficient	10^{-10} sec^{-1}
Cell size in the leaf upper half	8 μm x 32 cells
Cell size in the leaf lower half	8 μm x 17 cells, 7 μm x 1 cell, 6 μm x 1 cell, 5 μm x 1 cell, 4 μm x 15 cells
Boundary edge intensity	0.3 a.u.

Table S2. Parameters used in the diffusion and growth simulation for the AN3-GFP gradient formation.

Time constant	25 min
Duration of cell cycle	16 hours (1,2)
Cell division	3 times
Source cell number	4 cells
Degradation coefficient	10^{-10} sec^{-1}
Cell size for constant cell-size field	4 μm constant
Cell size for differential cell-size field	4 μm x 1 cell, 5 μm x 1 cell, 6 μm x 1 cell, 7 μm x 1 cell, followed by 8 μm cells

Table S3. Parameters used in the diffusion and growth simulation for the AN3-GFP gradient formation with theoretically estimated 2xGFPs diffusivity.

Time constant	40 min
Duration of cell cycle	16 hours (1,2)
Cell division	3 times
Source cell number	4 cells
Degradation coefficient	10^{-10} sec^{-1}
Cell size for constant cell-size field	4 μm constant
Cell size for differential cell-size field	4 μm x 1 cell, 5 μm x 1 cell, 6 μm x 1 cell, 7 μm x 1 cell, followed by 8 μm cells

4. Movie S1. Recovery of GFP fluorescence in the square FRAP assay.

5. Supporting References

[1] Ichihashi, Y., Kawade, K., Usami, T., Horiguchi, G., Takahashi, T., and Tsukaya, H. 2011. Key proliferative activity in the junction between the leaf blade and leaf petiole of Arabidopsis. Plant Physiol. 157:1151-1162.

[2] Yin, K., Ueda, M., Takagi, H., Kajihara, T., Aki, S.S., Nobusawa, T., Umeda-Hara, C., and Umeda, M. 2014. A dual-color marker system for in vivo visualization of cell cycle progression in Arabidopsis. Plant J. 80:541-552.

[3] Kawade, K., Horiguchi, G., Usami, T., Hirai, M.Y., and Tsukaya, H. 2013. ANGUSTIFOLIA3 signaling coordinates proliferation between clonally distinct cells in leaves. Curr. Biol. 23:788-792.

[4] Kawade, K., Horiguchi, G., and Tsukaya, H. 2010. Non-cell-autonomously coordinated organ size regulation in leaf development. Development. 137:4221-4227.

[5] Ferjani, A., Horiguchi, G., Yano, S., Tsukaya, H. 2007. Analysis of leaf development in *fugu* mutants of Arabidopsis revealed three compensation modes that modulate cell expansion in determinate organs. Plant Physiol. 144:988-999.

[6] Kawade, K., and Tanimoto, H. 2015. Mobility of signaling molecules: the key to deciphering plant organogenesis. J. Plant Res. 128:17-25.

[7] Haberman, W.L., Sayre, R.M. 1958. Motion of rigid and fluid spheres in stationary and moving liquids inside cylindrical tubes. David Taylor Model Basin, Report 1143.